ACS OMEGA

Open Access

http://pubs.acs.org/journal/acsodf

Article

Supercapacitor Performance of Activated Carbon from *Eucommia Ulmoides* Oliver Wood Optimized by the Activation Method

Haitao Song,[⊥] Qiang Qu,[⊥] Zhuangzhuang Yang, Yanrong Zhang, Ling Qiu, Yibo Zhao, Chenguang Li, Mingqiang Zhu,* and Xuanmin Yang*

Cite This: *ACS Omega* 2025, 10, 15368−15380

Read Online

ACCESS | Metrics & More | Article Recommendations

ABSTRACT: Amid the growing demand for sustainable energy storage, biomass-derived porous carbons have emerged as eco-friendly alternatives to conventional electrode materials. This study shows that activated carbon prepared by one-step activation exhibits an enhanced specific surface area and pore volume. The optimum parameter for ameliorating the structural and electrochemical properties is 60 min of microwave heating. The specific surface area, pore volume, and mesopore volume of the resulting activated carbon (EUAC1−60) achieve 1589.0 m^2/g, 0.82 cm^3/g, and 0.28 cm^3/g, respectively. EUAC1−60 exhibits an exceptional defect degree with an I_D/I_G value of 0.92 and can provide ample active sites for ion storage. The electrochemical investigation shows that the EUAC1−60 electrode has the highest specific capacitance of 232.92 F/g at a current density of 0.2 A/g. In addition, continuous cycling performance at a current density of 1 A/g validates its exceptional stability with capacitance retention of 89.90% and Coulombic efficiency of 117.21% after 10,000 cycles. The zinc ion hybrid supercapacitor with the EUAC1−60 cathode and Zn foil anode displayed an excellent energy density performance of 95.58 W h/kg at a power density of 64,800 W/kg. This research presents an innovative approach to the fabrication of high-performance activated carbon electrode materials from *Eucommia Ulmoides* Oliver, demonstrating its promising potential in supercapacitor applications.

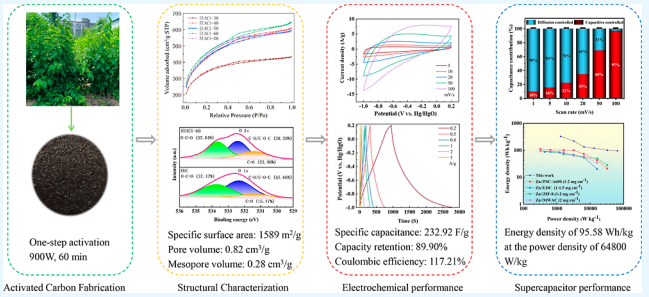

1. INTRODUCTION

Given the pressing global need for energy, dwindling fossil fuel reserves, and deteriorating environmental conditions, considerable attention should be given to enhancing the efficiency of energy storage and conversion apparatus.[1] Among the various energy storage devices available, rechargeable batteries (e.g., nickel metal hydride batteries and lithium ion batteries), conventional capacitors, and supercapacitors comprise the three primary categories. While rechargeable batteries commonly exhibit high energy density, their inferior power density and limited life prevent them from meeting the requirements for high power output and fast charging/discharging scenarios. Conventional capacitors, by contrast, were unable to satisfy the practical requirements due to their significantly low energy density.[2] Supercapacitors, in contrast, are swiftly evolving into potential energy storage technologies and are attracting considerable interest. These devices exhibit rapid charge−discharge velocity, exceptional circulation stability, and the ability to bridge the gap[3] between high-energy density cells[4] and traditional power density capacitors,[5] rendering them applicable in a broad array of sectors, encompassing telecommunications gear, hybrid vehicles,[6] smart grids, high-speed rail,[7] and spacecraft.[8] As a fundamental element of supercapacitors, electrode materials play a pivotal role and directly influence the electrochemical behavior of supercapacitors. Nevertheless, the exploration of novel electrode materials exhibiting superior performance, eco-friendly attributes, and low cost is an imperative issue to be addressed, which has considerably impeded the industrial development of supercapacitor devices.[9]

In the context of supercapacitor applications, an optimal electrode material is required to possess an appreciable specific surface area to absorb more electrolyte ions and augment its electrochemical functionality. Furthermore, the electrode material must also exhibit superior conductivity and rapid charge−discharge efficiency within a short duration. In light of these prerequisites, porous carbon, due to its adjustable morphology and superior conductivity, is deemed a promising supercapacitor electrode material.[10] Carbon-based electrode

Received: December 23, 2024
Revised: February 24, 2025
Accepted: March 28, 2025
Published: April 10, 2025

materials include graphene,[11] carbon nanotubes,[12] carbon nanofibers,[13] etc. Nonetheless, the intricate fabrication procedure and high costs have hindered their industrial application. On the contrary, biomass-derived activated carbon has emerged as a promising candidate for supercapacitor electrode composites due to its renewability,[14] substantial specific surface area,[15] exceptional electrochemical durability,[16] and superior conductivity.[17] Prior investigations have achieved considerable advancements in constructing porous carbon materials derived from diverse biomass resources such as bamboo, olive tree pruning residues, and hazelnut shell, among others.[18−20] Notably, activation and carbonization procedures used to develop electrodes using biomass feedstock can induce unique porous and layered pseudo graphite wall morphologies.[21] However, activated carbon used in supercapacitor electrodes should provide ample room for ion storage by micropores and a well-developed pathway for ion transfer by mesopores.[22] Therefore, the carbon electrodes should possess an optimal pore distribution, which can be achieved by optimizing the preparation and activation process.

H_3PO_4 is commonly used as an activator due to its ability to create activated carbon materials with an abundance of micropores and mesopores.[23] The choice of H_3PO_4 was strategically guided by its multifaceted advantages in sustainability, pore structure engineering, and electrochemical functionality. Unlike conventional alkaline activators (e.g., KOH) or metal salts (e.g., $ZnCl_2$), H_3PO_4 provides an environmentally benign activation pathway with minimal generation of corrosive byproducts, aligning with green chemistry principles while reducing postprocessing hazards.[24,25] Its unique activation mechanism, involving dehydration and cross-linking reactions at moderate temperatures ($\leq$500 °C), enables the simultaneous development of a hierarchical pore architecture: microporous domains to maximize charge storage capacity and mesoporous channels to facilitate rapid ion diffusion, thereby synergistically enhancing both specific capacitance and rate performance.[26−28] Furthermore, the phosphorus-containing functional groups (e.g., C−O−PO_3) introduced during H_3PO_4 activation not only improve interfacial wettability for efficient electrolyte penetration but also contribute to pseudocapacitance through reversible redox reactions.[29] The activating process is divided into one-step and two-step activation.[30] During one-step activation, biomass is impregnated with the activator prior to the carbonization process. The activator interacts directly with biomass by cleaving the aryl ether bonds. Concurrently, gas release is accelerated by dehydration and condensation mechanisms associated with hydrolyzed glycosidic bonds present in hemicellulose and cellulose.[31] In addition, phosphate and polyphosphate moieties are formed by H_3PO_4 conjugation with organic components within the biomass source, which subsequently facilitates the expansion of the precursor into the porous structure.[32] Alternatively, a two-step activation procedure involves carbonization and subsequent impregnation in the activator, followed by activation at an elevated temperature to produce activated carbon. Throughout the two-step activation protocol, pyrolysis results in the release of volatile components and facilitates the production of pores within activated carbon. However, certain tar constituents partially block the developed pores. The physicochemical characteristics of activated carbon generated by one-step versus two-step activation may show considerable differences, potentially affecting supercapacitors' performance. However, systematic investigations of the effects of these two methods on the physical and chemical properties of activated carbon are rarely conducted.

Eucommia Ulmoides Oliver (EUO) stands as a significant economic tree species exclusively found in China. The cultivated area of this species covers over 95% of the worldwide EUO resources, yielding substantial annual biomass assets.[33] However, improper use of these biomass resources can lead to serious resource wastage and environmental contamination dilemmas. Hence, there is a growing need to convert EUO wood into value-added products. Research efforts have been devoted to harnessing EUO wood as a sustainable precursor for high-performance supercapacitor electrodes, with a particular focus on structural and process optimization strategies. These endeavors encompass systematic investigations into pore structure engineering of biomass-derived activated carbons,[34] comparative analyses of thermal activation methodologies,[35,36] and mechanistic studies of H_3PO_4-mediated activation protocols.[37] However, critical knowledge gaps persist regarding the fundamental differences between one- and two-step activation approaches in governing the hierarchical porosity and charge storage behavior of EUO wood-derived carbons. A systematic understanding remains essential for rational design of biomass-based electrodes with tailored energy-power characteristics.

In this study, we have developed a method using both one- and two-step activation procedures with H_3PO_4 as a chemical activator to manufacture EUO activated carbon. The optimal activation technique (one-step or two-step activation) is selected based on the distinct pore structure of the activated carbon, and microwave heating technology is used to investigate the effects of heating time on the pore architecture characteristics of the activated carbon. By contrasting the structural differences between activated carbon and biochar, the intrinsic correlations between the structural properties of activated carbon and its electrochemical performance are unveiled. In a three-electrode system, the electrochemical performance of EUO activated carbon is evaluated using cyclic voltammetry (CV), galvanostatic charge−discharge [galvanostatic charge/discharge (GCD)], and electrochemical impedance spectroscopy (EIS), and key metrics such as specific capacitance, capacitance retention, Coulombic efficiency, and energy density of the activated carbon electrode material are obtained. This work initiates a sustainable strategy to transform underutilized EUO wood biomass into hierarchically porous carbons through H_3PO_4-microwave synergy, offering a dual advantage of coefficient fabrication and remarkable energy storage performance. Our findings not only advance the rational design of biomass-derived supercapacitor electrodes but also establish a model for converting agricultural forestry residues into high-value carbon materials for next-generation energy devices.

2. EXPERIMENTAL SECTION

2.1. Materials. The EUO wood used for this study was sourced from Yangling City, Shaanxi Province, China. The bark and foliage are carefully removed and subjected to a drying procedure at 105 °C for 24 h. The dried wood is then processed into a wood meal (40−60 mesh sizes). H_3PO_4 of analytical purity (99.90%) was purchased from Energy Co., Ltd. (Shanghai, China).

2.2. Preparation of Carbon Material via Microwave Heating. 6.00 g portion of feedstock is transferred to a 900 W

https://doi.org/10.1021/acsomega.4c11529
ACS Omega 2025, 10, 15368−15380

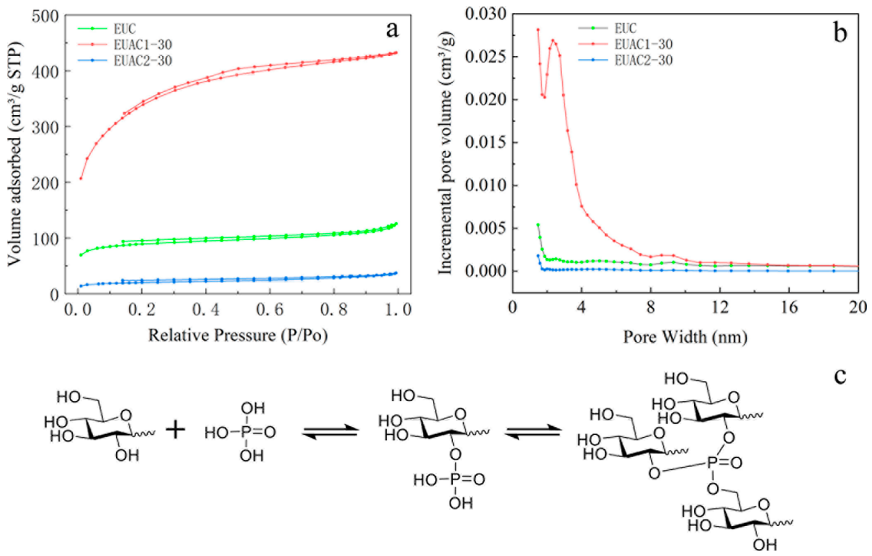

Figure 1. (a) N_2 adsorption−desorption isotherm and (b) pore diameter distribution of EUC, EUAC1−30 and EUAC1−30 and (c) chemical formula illustrating the formation of phosphate ester bond between phosphoric acid and biopolymer.

microwave heating reactor for 30 min. N_2 gas is introduced into the reactor at a rate of 200 mL/min throughout the heating process. After heating, the substance is treated with 0.1 M HCl and then rinsed repeatedly with deionized water until a neutral pH is reached. This final product is designated as EUC.

In a one-step activation process, 25 wt % phosphoric acid is used as a chemical activator. This process involves immersing 6.00 g of EUO wood meal in water for 9 h with a solid/liquid ratio of 1:4. After a 2 h drying period, the precursor undergoes a pyrolysis process in a microwave reactor. The resulting solid product is then washed to generate EUO activated carbon. Microwave heating time varies from 30 to 70 min, and the resulting activated carbon materials are named EUAC1−30, EUAC1−40, EUAC1−50, EUAC1−60, and EUAC1−70, respectively.

The two-step activation method involves using EUC as a starting material and subjecting it to a chemical activation process. The resultant material then undergoes a 30 min pyrolysis, followed by immersion in 0.1 M HCl and subsequent water washing to achieve a neutral pH prior to drying. The final product is denoted as EUAC2−30.

2.3. Characterization of Carbon Material. SEM-EDS (TM3000, Hitachi, Japan) is used to analyze the micro morphology and composition of our samples. A special surface area instrument (Tristar II 3020, Micromeritics, USA) is used to measure the surface area and pore diameter distribution to provide deeper insight into pore characteristics through using the multipoint N_2 adsorption−desorption process. These results are further determined through BET and DFT models. To determine the chemical properties of the surface, Fourier transform infrared (FT-IR) spectroscopy (Vertex70, Bruker, Germany) is performed over a wide spectral range of 400−4000 cm^{-1}. Activated carbon was further examined by XPS analysis using a Veresprobe II spectrometer operated under Al Ka radiation. To evaluate the crystallinity of the sample, XRD patterns were analyzed with a D8 ADVANCE A25 instrument (Bruker, Germany) via Cu-Ka radiation at 30 kV and 20 mA, all processed with JADE software (version 5.0). Raman spectral analysis was carried out using a sophisticated Raman microscope system (Horiba JobinYvon, Longjumeau, France), which incorporated a confocal microscope (Olympus BX51, Tokyo, Japan) together with a motorized X/Y sample stage. This equipment is coupled to an argon ion laser that operates at an optimal excitation wavelength of 532 nm for data collection.

2.4. Electrode Preparation and Electrochemical Assays. The working electrode is created by combining EMAC1−60, carbon black (SUPERT-P, TIMCAL), and polytetrafluoroethylene (PTFE, Aldrich) at a uniform weight ratio of 8:1:1. This blend is then coated on a stainless-steel mesh, with an active mass weight per unit area of ∼8.0 mg/$cm^2$and thickness of ∼0.05 mm.

The electrochemical characterization of the electrode is evaluated using EIS, cyclic voltammetry (CV), and GCD analysis in a three-electrode system under the potential window spanning from −1.0 to 0.2 V. A platinum foil functions as the counter electrode, and a Hg/HgO electrode serves as the reference electrode, with an aqueous 1 M KOH functioning as the electrolyte. The EIS technique was implemented on an electrochemical workstation (Zahner Im6ex). The applied frequency was between 100 kHz and 10 MHz, and the ac signal amplitude was 5 mV. The specific capacitance of activated carbon material is then calculated through GCD measurements at charge/discharge current densities ranging from 0.2 to 5 A/g and CV evaluation with varying scanning rates (5, 10, 20, 50, and 100 mV/s). The specific capacitance value (Cs, expressed in F/g) is determined from GCD using eq 1

$$C_s = I \times \Delta t/(m \times \Delta v) \quad (1)$$

C_s is calculated by CV curve from the following eq 2

$$C_s = Q/(2V \times m \times \Delta v) \quad (2)$$

where I denotes the current, Δt indicates the duration of the electrical discharge, m stands for the activated material's mass (g), Δv signifies the potential window (V), Q is fitting area of CV curve, and V is the scan rate (V/s).

When studying the storage behavior of EUAC1−60 for Zn^{2+} in depth, the correlation between scan rate (v) and peak current (I) can be expressed as follows

https://doi.org/10.1021/acsomega.4c11529
ACS Omega 2025, 10, 15368−15380

Table 1. Comparing the Specific Surface Area, Pore Volume, and Average Pore Diameter Obtained under Different Activation Methods

	S_{BET} (m^2/g)	S_{micro} (m^2/g)	S_{meso} (m^2/g)	V_{total} (cm^3/g)	V_{micro} (cm^3/g)	V_{meso} (cm^3/g)	D_{total} (nm)	P_{meso} (%)
EUC	292.8	157.0	135.8	0.14	0.09	0.05	2.61	35.71
EUAC1−30	1178.1	383.1	795.0	0.57	0.22	0.35	2.27	61.40
EUAC2−30	66.7	26.5	40.2	0.04	0.02	0.02	3.36	50.00

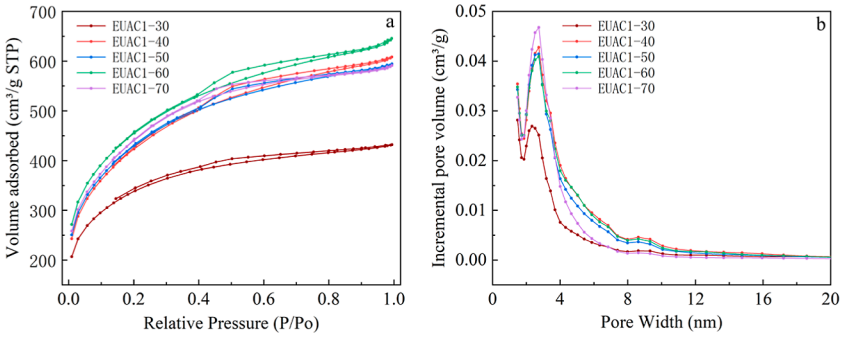

Figure 2. Effect of activation time on (a) N_2 adsorption−desorption isotherm and (b) pore diameter distribution through a one-step activation method.

$$i = av^b \tag{3}$$

where the parameter b value of 0.5 generally corresponded to slow reaction kinetics deaminated by surface diffusion, while the parameter b value of 1.0 denoted the ultrarapid reaction kinetics of capacitive behavior.

Furthermore, the *Dunn* method can be used to classify and quantify the proportions of the reaction contributions. The following equation illustrated the precise calculation process

$$\mathrm{i} = k_1\mathrm{v} + k_2v^{1/2} \tag{4}$$

where k_1v and $k_2v^{1/2}$ denoted the fraction of capacitive and diffusion contributions, respectively.

3. RESULTS AND DISCUSSION

3.1. Effect of the Activation Method on the Pore Structure. N_2 adsorption and desorption methods are used to evaluate the porosity profile of the sample. As demonstrated in Figure 1a, significant volumetric adsorption differences are observed for EUAC1−30 at low relative pressures of 0 and 0.2 P/P_0, suggesting a substantial increase in its adsorption capacity compared to both EUAC2−30 and EUC. This finding suggests that EUAC1−30 possesses a more complex microporous structure than EUAC2−30 and EUC. The corresponding micropore volumes (EUAC1−30:0.22 cm^3/g; EUAC2−30:0.02 cm^3/g; EUC: 0.09 cm^3/g) support this conclusion (Table 1). During N_2 adsorption and desorption, capillary condensation induces N_2 molecules to condense and occupy the mesoporous channels. Nitrogen adsorption occurs from the liquid interface of the pore wall, while desorption is initiated at the pore opening. Notably, the nitrogen adsorption and desorption paths do not align to form a hysteresis loop (Figure 1a). This observation indicates the presence of mesopores in the sample, similar to typical type IV adsorption/desorption patterns exhibiting a characteristic H4 hysteresis loop.[38] Specifically, EUAC1−30 exhibits a substantially elevated adsorption capacity in the medium pressure domain, accompanied by a pronounced hysteresis loop compared to both EUAC2−30 and EUC, indicating a more widespread distribution of mesoporous architecture throughout EUAC1−30. These results are consistent with the observed trends in the measured specific surface area and pore volume. The specific surface area (1178.1 m^2/g), total pore volume (0.57 cm^3/g), and mesopore volume (0.35 cm^3/g) of EUAC1−30 outperform those of EUAC2−30 (66.7 m^2/g, 0.04 cm^3/g, and 0.02 cm^3/g), along with those of EUC (292.8 m^2/g, 0.14 cm^3/g, and 0.05 cm^3/g).

The pore dimensionality of carbon can be profoundly altered by the choice of activation protocols. As illustrated in Figure 1b, the pore diameter of EUAC1−30 ranges from 1 to 8 nm, manifesting a significant prevalence of both micropores and mesopores when compared to those of EUC and EUAC2−30. This disparity may result from differences in their phosphoric acid activation strategies (i.e., one- vs two-step). The one-step method integrates phosphoric acid directly into biomass. The substantial hydroxyl function groups within hemicellulose and cellulose facilitate the penetration and flow of phosphoric acid across the substrate. This results in a beneficial dispersion structure, significantly influencing the subsequent formation of pore architecture. During the subsequent thermal decomposition step, phosphoric acid cross-links with the biopolymer (Figure 1c). The covalent reaction involves condensation of three hydroxyl entities in phosphoric acid with hydroxyl units in polysaccharides, leading to the formation of phosphate ester bonds. This bond prevents cell wall shrinkage during thermal decomposition and is a critical stage in the genesis of mature pore architectures.[39] Finally, after cleaning activated carbon, both phosphoric acid and its phosphoric-acid-biomass complex are eliminated, yielding pores of diverse dimensions in the final activated carbon. However, the two-step activation procedure can result in activated carbon with increased crystallinity, impeding phosphoric acid's ability to copolymerize with the carbon framework, leading to suboptimal penetration.[40] In cases where the diminished oxygen functional groups act as a significant obstacle to the effective intercalation of phosphoric acid, this is clearly manifested by the restricted pore development observed in EUAC2−30, as documented in Table 1. Findings from this study are in alignment with the research by Fang et al. (2013) and Ma et al. (2014), which indicates that the delayed

https://doi.org/10.1021/acsomega.4c11529
ACS Omega 2025, 10, 15368−15380

Table 2. Pore-Associated Parameters under Varying Activation Times

	S_{BET} (m^2/g)	S_{micro} (m^2/g)	S_{meso} (m^2/g)	V_{total} (cm^3/g)	V_{micro} (cm^3/g)	V_{meso} (cm^3/g)	D_{total} (nm)	P_{meso} (%)	yield (%)
EUAC1−30	1178.1	383.1	795.0	0.57	0.22	0.35	2.27	61.40	54.07
EUAC1−40	1498.8	450.2	1048.7	0.80	0.24	0.56	2.51	70.00	52.24
EUAC1−50	1510.4	474.5	1035.9	0.81	0.25	0.56	2.43	69.16	48.35
EUAC1−60	1589.0	522.8	1066.2	0.82	0.28	0.54	2.51	65.85	42.12
EUAC1−70	1559.2	526.7	1032.4	0.77	0.26	0.51	2.34	66.23	38.86

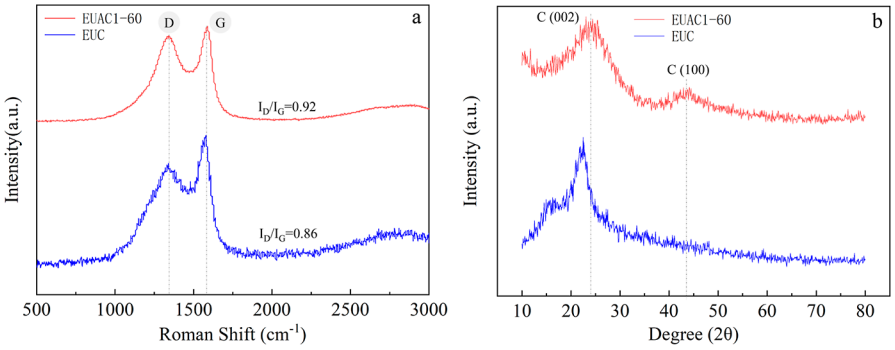

Figure 3. Raman spectrum (a) and XRD (b) of EUC and EUAC1−60.

introduction of the activator leads to a reduction in the Lewis acid−base interactions that are crucial for the templating of mesopores. This disruption can have a profound impact on the pore structure formation.[41,42] The outstanding capacitance retention rate of 89.90% achieved under high-rate cycling can be attributed to the optimal hierarchical porosity obtained through the one-step activation method. As elaborated by Khalil et al. (2021) and Meng et al. (2023), the interconnected mesopores play a pivotal role in alleviating the ion diffusion bottlenecks that are typically encountered in purely microporous carbons.[43,44] This unique structural feature ensures efficient ion transport and contributes significantly to the enhanced electrochemical performance. Therefore, compared to the two-step activation protocol, the one-step activation method produces activated carbon with superior pore architecture, specific surface area, micropore volume, and mesopore volume, making it more conducive to electrolyte permeation during the battery charge and discharge process.

3.2. Effect of Activation Time on the Porosity Structure. The activation time has a great impact on the penetration of phosphoric acid into the carbon precursor and the porosity of the activated carbon material. However, this has rarely been studied in detail. To reach this goal, a one-step activation procedure involving a 900 W microwave for variable durations of 30, 40, 50, 60, and 70 min is applied. Representative N_2 adsorption−desorption isotherms and pore diameter distribution are illustrated in Figure 2. As shown, all samples exhibit type IV adsorption isotherms, indicating a high abundance of micropores and mesopores in the carbon material (Figure 2a). The initial enhancement of the specific surface area from 1178.1 m^2/g (30 min) to 1589.0 m^2/g (60 min) can be attributed to progressive acid penetration and controlled etching of the carbon matrix. This aligns with the mechanism proposed by Wang et al.,[45] where extended activation facilitates deeper H_3PO_4 diffusion into biomass precursors, promoting simultaneous micropore formation and mesopore widening. While the adsorption capacity of the samples initially increased with prolonged activation time, it then decreased slightly, suggesting that a prolonged activation time enhances the N_2 adsorption capacity of activated carbon. This finding is consistent with trends in the specific surface area and total pore volume (Table 2). However, excessive activation time can disrupt the pre-existing pore structure, the collapse of the porous network and pore blockage, thereby reducing the adsorption ability.[46] The activation process resulted in a maximum specific surface area (1589.0 m^2/g), total pore volume (0.82 cm^3/g), and microporous pore volume (0.28 cm^3/g) over a 60 min period. In addition, the activation time significantly influences the average pore diameter variation of total pores in the activated carbon material. As shown in Figure 2b, the pore size of samples generally falls within 1−10 nm, with 2−4 nm mesopores contributing the most. In particular, EUAC1−60 displays the most advanced pore structure development. Thus, a 60 min activation time is considered optimal for converting EUO to activated carbon material through a one-step activation method.

3.3. Structural Characterization of EUC and EUAC1−60. The Raman spectrum is used to quantify the degree of disorder and crystalline properties of carbon samples. Both EUC and EUACI-60 display discernible peaks D and G. The peak at 1340 cm^{-1} corresponds to the lattice defects of carbon atoms, while peak G at 1580 cm^{-1} represents the inplane contraction vibration of sp^2 carbon atoms (Figure 3a). The ratio between the intensity of the D-band and G-band typically indicates the level of graphitization.[47] Notably, EUAC1−60 demonstrates a higher I_D/I_G ratio of 0.92 compared to 0.86 for EUC, revealing that the chemical activation process effectively introduces topological defects and disrupts the long-range graphitic order. The increased defect density in EUAC1−60 can be attributed to two synergistic effects: (1) the one-step activation etches carbon skeletons to form hierarchical pore channels, as evidenced by the enhanced specific surface area in BET analysis; (2) the interfacial defects at crystallite boundaries promote the formation of interconnected ion transport pathways.[48,49] In addition, EUACI-60 exhibits a superior degree of defect at the material interface, potentially facilitating interconnected channel structures for the rapid adsorption and desorption of electrolyte ions. This advantage would contribute to minimal internal resistance (IR) and

https://doi.org/10.1021/acsomega.4c11529
ACS Omega 2025, 10, 15368−15380

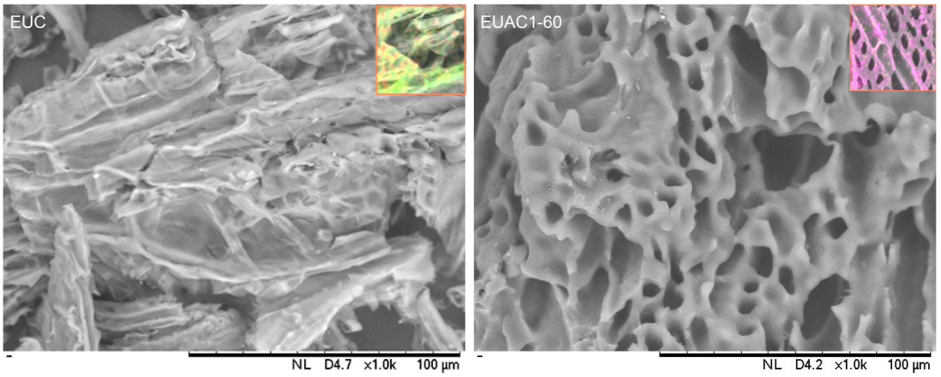

Figure 4. SEM and EDS images of EUC and EUAC1−60.

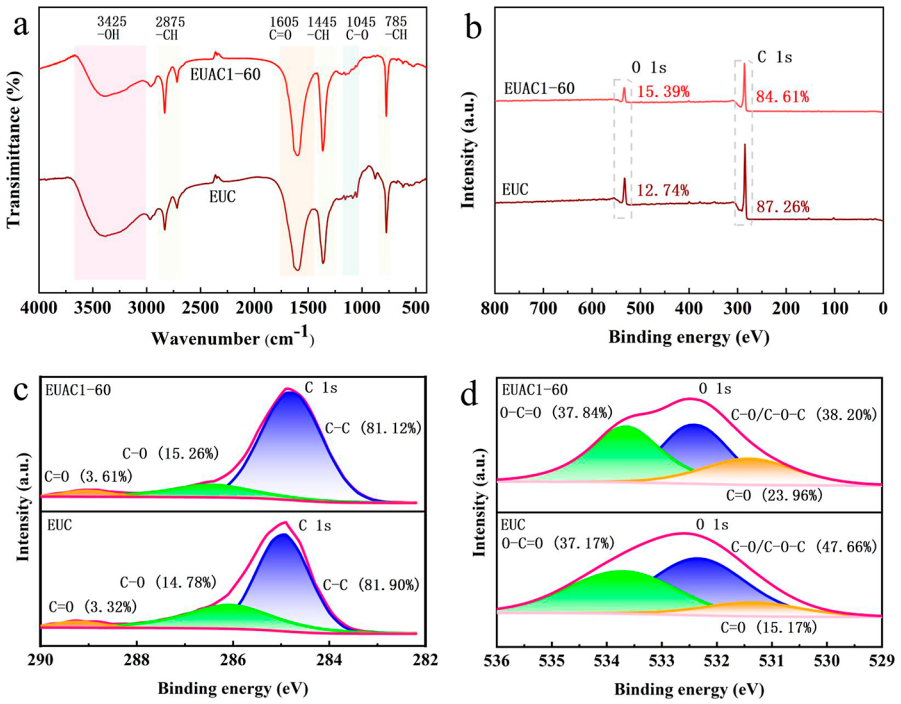

Figure 5. FT-IR and XPS spectra of EUC and EUAC1−60. (a) FTIR spectrum, (b) XPS survey, (c) C element high-resolution spectrum, and (d) O element high-resolution spectrum.

enhanced rate performance during the electrochemical reaction of carbon electrodes.

Furthermore, XRD spectroscopy was employed to further investigate the crystal structure of all of the samples, as illustrated in Figure 3b. Two distinct peaks, corresponding to (002) and (100) lattice planes, were clearly present at 22−26 and 42−46°. Compared to the sharp and narrow peak in the EUC spectrum, EUAC1−60 exhibits a reduced intensity and considerable breadth, suggesting the minimal graphitization and crystallization.[50] These findings correlate well with the abundant defect structure observed in the Raman analysis results. This phenomenon may be attributed to phosphoric acid etching, which damages the uniform, flaky crystal framework present within the EUO wood. This process could yield a more diversified pore architecture and an increase in the specific surface area of the amorphous activated carbon, thereby facilitating the charge storage capacity and amplifying the specific capacitance. These results support the analysis of N_2 adsorption−desorption isotherm and pore size distribution curves, demonstrating the appropriate activation time (60 min) for fortifying structural properties.

SEM analysis is performed to examine the morphology and microstructure of the carbon samples. SEM images (Figure 4) show that a EUAC1−60 s surface area is rougher than that of EUC, indicating that it undergoes a more intense reaction during the one-step activation process. The pore structure of EUAC1−60 is significantly different from that of EUC. The pore structure of EUAC1−60 showed an increased presence of pores and a reduced graphite layer than EUC. As corroborated in Raman and XRD analysis, the pore structure of EUAC1−60 showed signs of rupture, potentially leading to pore expansion of existing pores. Furthermore, EDS technology is used to examine the distribution of elements on the material surface. The analysis shows that the carbon content of EUAC1−60 (81.98%) is lower than that of EUC (84.84%). This discrepancy could be explained by the consumption of carbon in the precursor during the activation process, which potentially facilitates the progression of the pore development.

https://doi.org/10.1021/acsomega.4c11529
ACS Omega 2025, 10, 15368−15380

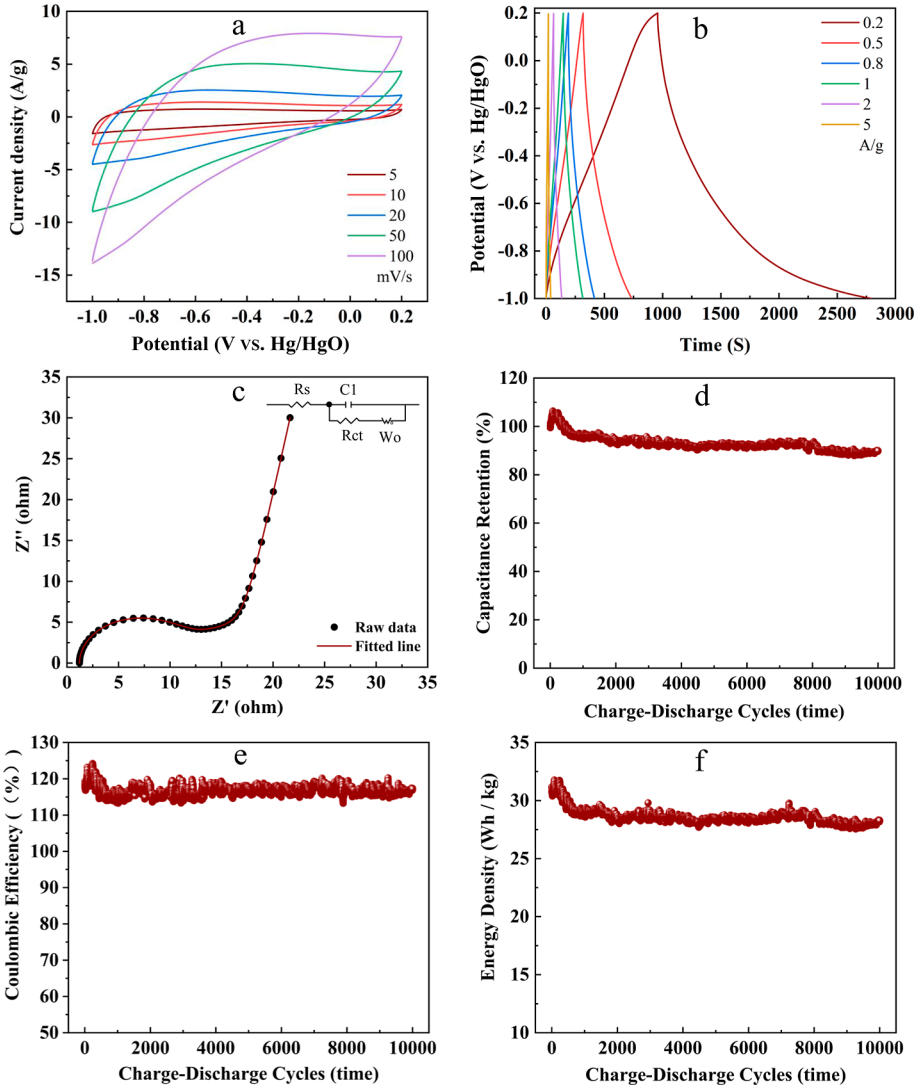

Figure 6. Electrochemical efficiency of EUAC1−60. (a) CV curves with varying sweep rates, (b) GCD curves with diverse current density, (c) EIS spectrum, and (d−f) long cycling performance.

The chemical composition of carbon materials can significantly affect the electrode−electrolyte interface reaction. The FT-IR technique is employed to scrutinize the oxygen-bearing functional groups within EUC and EUAC1−60. In the spectrum, the broad band within the range of 3500−3300 cm^{-1} could be attributed to the −OH group, whereas the adsorption bands at 1045 cm^{-1} are ascribed to the stretching vibration of the C−O bond.[51] In addition, there are strengthened bands of −CH (2875, 1445, and 785 cm^{-1}) and C═O (1605 cm^{-1}) groups appearing in the EUAC1−60 spectrum. This property is advantageous for the hydrophilicity of carbon electrodes in the three electrode system, thus further enhancing the transmission of electrolyte ions in the pores of the activated carbon material.

Furthermore, the relative content of chemical bonds on the carbon material surface was further investigated by using the XRS spectrum. The total survey and fitted core-level XPS spectra showed that C and O are the main surface elements of both the samples. In detail, the relative content of O element (15.39%) on the EUAC1−60 surface is higher than that (12.74%) on EUC in Figure 5b, and the trend of C element was opposite. This may be due to the intensive cross-link reaction between phosphoric acid and biomass precursor, and the consumption of carbon compounds to generate abundant pore structure.[52] Specifically, the high-resolution spectra of the C element are deconvoluted into C−C (284.8 eV), C−O (285.7 eV), and C═O (288.7 eV) by the Gaussian method, and the O element spectra are contributed to C═O (531.6 eV), C−O/C−O−C (533.2 eV), and O−C═O (533.8 eV) (Figure 5c and d). Besides, EUAC1−60 exhibits the higher relative content of O−C═O and C═O groups than these on EUC. This phenomenon suggests that the activation of phosphoric acid could not only create numerous pore structure and defect sites, but improve the reaction activity of material surface. It is undeniable that it shall further augment the electrochemical efficiency of the carbon electrode through reinforcing the specific capacitance and mitigating the resistance of ion transmission.

3.4. Electrochemical Performance of EUAC1−60. As shown in Figure 6a, at a scanning speed of 5 mV/s, the specific capacitance of the EUAC1−60 electrode exceeds 230 F/g. This is primarily due to the fact that at lower scanning speeds the electrolyte has sufficient time to permeate the mesopore structure, thus enhancing the utilization of micropores and

https://doi.org/10.1021/acsomega.4c11529
ACS Omega 2025, 10, 15368−15380

Table 3. Specific Capacitance of EUAC1-60 and Currently Reported Porous Carbon Materials

material	electrolyte	specific capacitance	stability	ref
NaOH-activated carbon	1 M H_2SO_4	125.9 F/g at 1 A/g		54
AC−Si	1.5 M KOH	141 F/g at 0.5 A/g		55
ACFS	3 M KOH	115.3 F/g at 1 A/g		56
N-doped RHAC/GCE	1 M KCl	121 F/g at 0.2 A/g	94.6% after 1000 cycles	61
AJSPC&Ti-A	1 M Na_2SO_4	156.1 F/g at 0.5 A/g	75% after 5000 cycles	62
iron-doped CSPP	6 M KOH	131.7 at 0.2 A/g		63
$Ti_3C_2Tx/CDs@MnO_2$	6 M KOH	124.6 F/g at 1 A/g	82.38% after 10,000 cycles	64
$Ti_3C_2T_x/Li_2Mn_3ZnO_8$	3 M KOH	182 F/g at 1 A/g	71% after 3000 cycles	65
AFO100	3 M KOH	229.71 F/g at 1 A/g	82.99% after 1000 cycles	66
AC	6 M KOH	160 F/g at 0.5 A/g	101% after 3000 cycles	67
HLSPC-2	1 M H_2SO_4	486 F/g at 0.5 A/g	85% after 10,000 cycles	68
EUAC1−60	1 M KOH	232.92 F/g at 0.2 A/g	89.90% after 10,000 cycles	this work

promoting the generation of double-layer capacitance. As the scanning speed increases, the area covered by the cyclic voltammetry curve gradually expands and deviates from a rectangular shape. This deviation primarily stems from the RC time constant. A longer RC time constant results in a prolonged transition stage during voltage conversion, which results in a sluggish alteration of the curve bias when switching scanning direction.[53] Despite the increase in scanning speed, at 100 mV/s, the CV profile of the EUAC1−60 electrode still exhibits an excellent quasi-rectangular shape, indicating its innate characteristics of rapid charge and discharge and desirable double-layer capacitance performance. The observed exceptional electrochemical performance can be ascribed to the sample's intricate pore structure, which facilitates rapid ion transport.

In Figure 6b, GCD curves of different current densities are illustrated. Activated carbon samples with higher micropore volumes are more conducive to storing electrolyte ions and play a pivotal role in the electrode electrochemical capacity. According to Formula 1, the specific capacitance rate at current densities of 0.2, 0.5, 0.8, 1, 2, and 5 A/g is as follows: 232.92, 153.17, 138.30, 131.42, 111.08, and 80.00 F/g, respectively. These values exceed or match those of other activated carbon electrodes derived from a variety of biomasses. For instance, a NaOH activated electrode from the biomass residues of date palm fronds exhibits 125.9 F/g specific capacitance at a current density of 1 A/g;[54] activated carbon coated by silica from olive stones exhibited 141 F/g specific capacitance at 0.5 A/g current density;[55] activated carbon fibers prepared from the natural cattail fibers via carbonization and subsequent chemical activation displays a specific capacitance of 115.3 F/g at 1 A/g current density.[56] This result indicates that EUAC1−60 exhibits an excellent specific capacitance property, which is mainly attributed to its superior graded-pore structure, where meso- and micropores coexist and interconnect. Micropores serve as storage spaces for electrolyte ions. The presence of mesopores can facilitate unimpeded pathways for ions to adsorb to active sites within the micropores.[57] The robustly constructed pore structure network in EUAC1−60 is capable of reducing the ion transfer route, thereby augmenting the ion transfer rate. In addition, at the initial stage of the GCD curves, there exists a marginal potential decline, which is primarily attributed to the presence of IR. At current densities of 0.2, 0.5, 0.8, 1, 2, and 5 A/g, changes in IR-induced potential drop are recorded as 0.02, 0.04, 0.06, 0.08, 0.15, and 0.36 V, respectively, which is correlated with increased diffusion resistance of electrolyte ions in microporous structures at elevated current density.[58]

To elucidate the intrinsic mechanisms of charge transfer, ion diffusion, and capacitance characteristics in activated carbon electrodes, EIS tests are conducted. As shown in Figure 6c, the EIS spectrum is divided into three distinct regions that correspond to high frequency, medium frequency, and low frequency. The half-circular shape reflects the resistance of the solution and mass transfer, while a 45° line observed in the middle frequency range indicates the diffusion velocity at the interface between the solution and the material. A straight line within the low-frequency band, corresponding to the Warburg impedance, mirrors the capacitive behavior of the electrode.[59] Using Z-View software, the EIS curve of EUAC1−6 is then fitted with equivalent circuit models. In detail, there is an EIS curve in the low-frequency range near perpendicular to the X axis, suggesting that the electrolyte solution can easily penetrate the porous structure of the activated carbon sample. Additionally, according to the equivalent circuit results, the electrolyte solution resistance (R_s) is 1.21 Ω, the charge transfer resistance (R_{ct}) is 9.48 Ω, and the Warburg impedance (W_o) is 0.45 Ω. These findings highlight the critical role of the sample's porous structure in ensuring rapid ion transport during the charging and discharging process, contributing significantly to the sample's exceptional impedance performance.

The cycling stability of carbon electrodes directly affects the performance of the application. At a current density of 1 A/g, EUAC1−60 exhibits 89.90% capacitance retention (Figure 6d), 117.21% Coulombic efficiency (Figure 6e), and energy density fluctuates between 31.18 and 28.26 W h/kg (Figure 6f). These results indicate that activated carbon obtained by one-step phosphoric acid activation exhibits good cycle stability, potentially due to the formed pore structure provides advantageous diffusion pathways for electrolyte ions. Therefore, it is concluded that activated carbon with a high pore volume is capable of relaxing volumetric and structural changes during the charge−discharge process, thereby achieving superior capacitance retention.[60]

The empirical data presented heretofore ensure that the EUAC1−60 electrode possesses superior electrochemical attributes. As depicted in Table 3, the capacitance and cycling stability of various electrode materials, encompassing a diverse array of biomass-based porous carbon materials, are meticulously documented. An analysis of Table 3 reveals that the energy storage capabilities of the EUAC1−60 electrode surpass those reported in numerous extant studies.[61−65] Nonetheless,

https://doi.org/10.1021/acsomega.4c11529
ACS Omega 2025, 10, 15368−15380

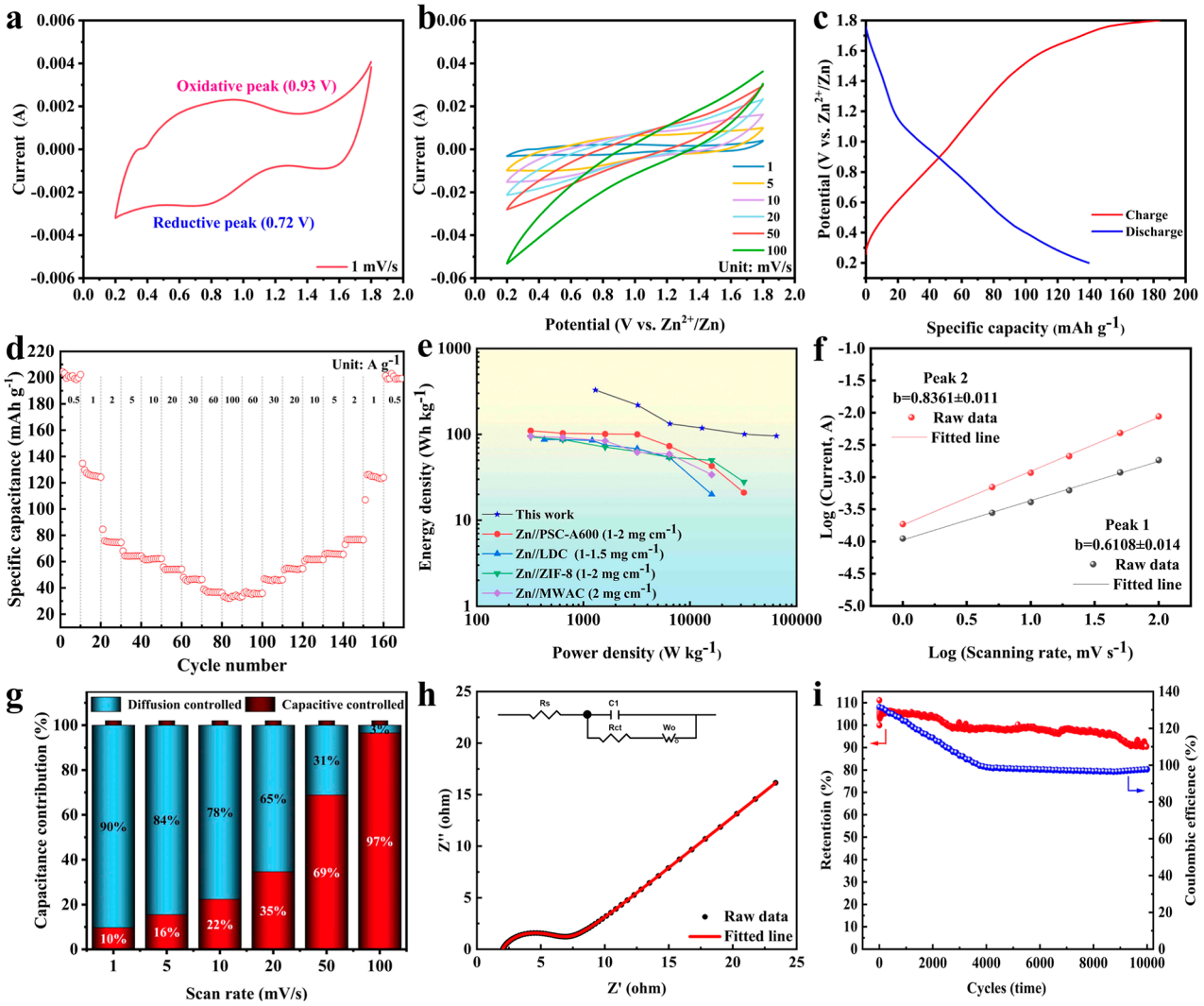

Figure 7. Zinc ion hybrid supercapacitor performance of EUAC1−60. CV curves (a) at the scanning rate of 1 mV/s and (b) at different scanning rates, (c) charging−discharging curve of EUAC1−60 in ZiHSC, (d) rate performance at the various current densities, (e) comparison of energy density with previous studies, (f) *b*-values of anode peak current and cathode peak current, (g) contribution rate of capacitive controlled kinetics at the scan rate of 1 mV/s, (h) EIS spectrum, and (i) capacitance retention rate and Coulombic efficiency for 10,000 cycles.

it is imperative to acknowledge that, when contrasted with a select few biomass-based porous carbon materials,[66−68] the electrochemical properties of EUAC1−60 continue to exhibit potential for enhancement.

3.5. Zinc Ion Hybrid Supercapacitor Performance of EUAC1−60. The zinc ion storage performance of the EUAC1−60 electrode was tested using the CV method at various scanning rates, and the curves are shown in Figure 7a and b. In detail, a pair of slight redox peaks (+0.72/0.93 V vs SHE) appeared on the curve at the scanning rate of 1 mV/s (Figure 7a), implying the storage behavior of Zn/Zn^{2+} by adsorption/desorption reaction within this voltage range. This phenomenon indicated that the electrochemical capacitance was mainly generated in the form of EDLC. As the scanning rate increased, the CV curves still maintained the rectangular shape and displayed the gradual shift of redox peaks toward the anodic and cathodic potential (Figure 7b). This trend suggested the synergistic storage mechanism of EDLC and faradic capacitance with the embedding and deposition of Zn/Zn^{2+} on the cathode. This advantage underscored the exceptional potential of EUAC1−60 as an electrode material for zinc ion hybrid supercapacitor (ZISC).

The discharging/charging profiles at a current density of 0.1 A/g of EUAC1−60 cathode are illustrated in Figure 7c. The EUAC1−60 cathode delivered an initial discharge capacity of a remarkable 139.43 mA h/g and a 131.7% coulomb efficiency. Furthermore, the rate performance of EUAC1−60 at various current densities was systematically evaluated. Specifically, it was first cycled 10 times at a current density of 0.1 A/g and then tested with the progressively augmented current density until 10 A/g (Figure 7d). Significantly, the electrochemical capacity can be retrieved to its initial value when the current density is returned to 0.1 A/g, indicating the exceptional rate performance of the EUAC1−60 cathode. This could be attributed to the well-developed Zn/Zn^{2+} diffusion pathways and excellent kinetics of charge transfer. Additionally, to evaluate the advantages of EUAC1−60 cathode, the electrochemical competency was compared with the earlier studies, and this study delivered the distinct advantages with energy density of 95.58 W h/kg at the power density of 64,800 W/kg (Figure 7e).[69−72]

https://doi.org/10.1021/acsomega.4c11529
ACS Omega 2025, 10, 15368−15380

To gain deeper insight into the Zn^{2+} storage behavior of EUAC1−60, the CV curves at different scanning rates were studied in detail. The correlation between the scan rate (v) and peak current (I) can be represented by eq 3. The b-values of anode peak current and cathode peak current on the EUAC1−60 cathode were specifically 0.8361 ± 0.011 and 0.6108 ± 0.014, indicating the predominant Zn^{2+} storage behavior by capacitive behavior (Figure 7f). According to reaction eq 4, it can be inferred that the contribution rate of capacitive controlled kinetics on the EUAC1−60 cathode at the scan rate of 1 mV/s was only 10% (Figure 7g). With the increase of scanning rate to 100 mV/s, the EUAC1−60 cathode displayed the superiority of ultrarapid electrochemical reaction with the capacitive behavior proportion of 97.3%.

Furthermore, the EIS measurements were conducted at open-circuit potentials across a frequency spectrum spanning from 100 kHz to 10 mHz to uncover potential mechanisms of ion transfer, charge diffusion, and capacitance formation. The Nyquist plots of the EUAC1−60 cathode illustrated the typical feature of a quasi-semicircle in the high frequency zone and a slash in the low frequency region (Figure 7h). Generally, the X-axis intercept of high-frequency (>10 Hz) graphs typically indicated the intrinsic ohmic resistance (R_s), while the diameter of the semicircle represented the charge-transfer resistance (R_{ct}). Besides, the raw data were fitted using an equivalent circuit model, and the low values of R_s (2.21 Ω) and R_{ct} (4.63 Ω) fitting parameters demonstrated the kinetic superiority of EUAC1−60 cathode.

In addition, with 10,000 cycles of repeated GCD testing at a current density of 1 A/g, EUAC1−60 still preserved 93.7% (Figure 7i), underscoring its robust porous architecture and exceptional surface chemistry. Consequently, the electrode material EUAC1−60 could emerge as an outstanding candidate for a superior ZISC.

4. CONCLUSIONS

This study demonstrates the rational fabrication of *E. ulmoides* Oliver wood-derived activated carbon (EUAC) through a systematic investigation, yielding three pivotal advancements. First, the proposed one-step microwave activation method exhibits superior controllability over pore architecture compared to conventional two-step approaches. By optimization of the pyrolysis duration to 60 min, the EUAC1−60 material achieves exceptional surface characteristics, including a BET-specific surface area of 1589.0 m^2/g, a total pore volume of 0.82 cm^3/g, and a micropore volume of 0.28 cm^3/g. Second, structural analyses reveal that the enhanced defect density (I_D/I_G ratio of 0.92) creates favorable ion-storage sites, directly translating to remarkable electrochemical performance. The material demonstrates outstanding cyclic stability with 89.90% capacitance retention and 117.21% Coulombic efficiency over 10,000 cycles, alongside a notable specific capacitance of 232.92 F/g at 0.2 A/g in a three-electrode configuration. Notably, practical implementation in zinc-ion hybrid supercapacitors delivers remarkable energy-power synergy, achieving 95.58 Wh/kg at a high power density of 64,800 W/kg. These findings establish a paradigm for defect-engineered carbon architectures derived from sustainable biomass precursors, offering a novel strategy for designing high-performance energy storage materials through the precise control of pore topology and defect chemistry. The work highlights the viability of EUAC as a competitive candidate for next-generation supercapacitors, while advancing green synthesis methodologies in functional carbon materials.

AUTHOR INFORMATION

Corresponding Authors

Mingqiang Zhu − *College of Mechanical and Electronic Engineering, Northwest A&F University, Yangling, Shaanxi 712100, P. R. China; Western Scientific Observing and Experimental Station for Development and Utilization of Rural Renewable Energy, Ministry of Agriculture and Rural Affairs, Yangling, Shaanxi 712100, P. R. China;* Email: zmqsx@nwsuaf.edu.cn

Xuanmin Yang − *College of Mechanical and Electronic Engineering, Northwest A&F University, Yangling, Shaanxi 712100, P. R. China; Western Scientific Observing and Experimental Station for Development and Utilization of Rural Renewable Energy, Ministry of Agriculture and Rural Affairs, Yangling, Shaanxi 712100, P. R. China;* Email: yangxuanmin@nwsuaf.edu.cn

Authors

Haitao Song − *College of Chemistry & Pharmacy, Northwest A&F University, Yangling, Shaanxi 712100, P. R. China*

Qiang Qu − *College of Mechanical and Electronic Engineering, Northwest A&F University, Yangling, Shaanxi 712100, P. R. China; Western Scientific Observing and Experimental Station for Development and Utilization of Rural Renewable Energy, Ministry of Agriculture and Rural Affairs, Yangling, Shaanxi 712100, P. R. China*

Zhuangzhuang Yang − *China Aerospace Science and Industry Corp Space, Wuhan, Hubei 431400, P. R. China*

Yanrong Zhang − *College of Chemistry & Pharmacy, Northwest A&F University, Yangling, Shaanxi 712100, P. R. China;* orcid.org/0000-0002-5641-3539

Ling Qiu − *College of Mechanical and Electronic Engineering, Northwest A&F University, Yangling, Shaanxi 712100, P. R. China; Western Scientific Observing and Experimental Station for Development and Utilization of Rural Renewable Energy, Ministry of Agriculture and Rural Affairs, Yangling, Shaanxi 712100, P. R. China*

Yibo Zhao − *College of Mechanical and Electronic Engineering, Northwest A&F University, Yangling, Shaanxi 712100, P. R. China*

Chenguang Li − *College of Mechanical and Electronic Engineering, Northwest A&F University, Yangling, Shaanxi 712100, P. R. China*

Complete contact information is available at: https://pubs.acs.org/10.1021/acsomega.4c11529

Author Contributions

⊥H.S. and Q.Q. contributed equally to this work.

Notes

The authors declare no competing financial interest.

ACKNOWLEDGMENTS

This work is supported by Xianyang Key R&D Program (L2023-ZDYF-XCZX-003), the National Key R&D Program of China (2024YFD1700500), Agricultural Key-scientific and Core-technological Project of Shaanxi Province (2024NYGG011), Xian yang Qin chuang yuan Science and Technology Innovation Project (L2022-QCYZX-GY-016), and

the Ministry of Education's Cooperative Education Project (231107541235424,231107541242397).

REFERENCES

(1) Mao, Y.; Xie, H.; Chen, X.; Zhao, Y.; Qu, J.; Song, Q.; Ning, Z.; Xing, P.; Yin, H. A combined leaching and electrochemical activation approach to converting coal to capacitive carbon in molten carbonates. *J. Clean Prod.* **2020**, *248*, 119218.
(2) Abioye, A. M.; Ani, F. N. Recent development in the production of activated carbon electrodes from agricultural waste biomass for supercapacitors: A review. *Renewable Sustainable Energy Rev.* **2015**, *52*, 1282−1293.
(3) Zhang, G.; Chen, Y.; Chen, Y.; Guo, H. Activated biomass carbon made from bamboo as electrode material for supercapacitors. *Mater. Res. Bull.* **2018**, *102*, 391−398.
(4) Cossutta, M.; Vretenar, V.; Centeno, T. A.; Kotrusz, P.; McKechnie, J.; Pickering, S. J. A comparative life cycle assessment of graphene and activated carbon in a supercapacitor application. *J. Clean Prod.* **2020**, *242*, 118468.
(5) Ghosh, A.; Razzino, C. d. A.; Dasgupta, A.; Fujisawa, K.; Vieira, L. H. S.; Subramanian, S.; Costa, R. S.; Lobo, A. O.; Ferreira, O. P.; Robinson, J.; et al. Structural and electrochemical properties of babassu coconut mesocarp-generated activated carbon and few-layer graphene. *Carbon* **2019**, *145*, 175−186.
(6) Wang, J.; Zhang, X.; Li, Z.; Ma, Y.; Ma, L. Recent progress of biomass-derived carbon materials for supercapacitors. *J. Power Sources* **2020**, *451*, 227794.
(7) Wu, C.; Zhang, S.; Wu, W.; Xi, Z.; Zhou, C.; Wang, X.; Deng, Y.; Bai, Y.; Liu, G.; Zhang, X.; et al. Carbon nanotubes grown on the inner wall of carbonized wood tracheids for high-performance supercapacitors. *Carbon* **2019**, *150*, 311−318.
(8) González, A.; Goikolea, E.; Barrena, J. A.; Mysyk, R. Review on supercapacitors: Technologies and materials. *Renewable Sustainable Energy Rev.* **2016**, *58*, 1189−1206.
(9) Ding, W.; Xiao, L.; Lv, L. P.; Wang, Y. Redox-Active Organic Electrode Materials for Supercapacitors. *Batteries Supercaps* **2023**, *6* (11), No. e202300465.
(10) Sevilla, M.; Mokaya, R. Energy storage applications of activated carbons: supercapacitors and hydrogen storage. *Energy Environ. Sci.* **2014**, *7* (4), 1250−1280.
(11) Iqbal, M. F.; Ashiq, M. N.; Hassan, M.-U.; Nawaz, R.; Masood, A.; Razaq, A. Excellent electrochemical behavior of graphene oxide based aluminum sulfide nanowalls for supercapacitor applications. *Energy* **2018**, *159*, 151−159.
(12) He, S.; Hu, Y.; Wan, J.; Gao, Q.; Wang, Y.; Xie, S.; Qiu, L.; Wang, C.; Zheng, G.; Wang, B.; et al. Biocompatible carbon nanotube fibers for implantable supercapacitors. *Carbon* **2017**, *122*, 162−167.
(13) Wang, L.; Huang, M.; Chen, S.; Kang, L.; He, X.; Lei, Z.; Shi, F.; Xu, H.; Liu, Z.-H. δ-MnO2nanofiber/single-walled carbon nanotube hybrid film for all-solid-state flexible supercapacitors with high performance. *J. Mater. Chem. A* **2017**, *5* (36), 19107−19115.
(14) Shatla, A. S.; Abd-El-Latif, A. A.; Ayata, S.; Demir, D.; Baltruschat, H. Iodide adsorption at Au(111) electrode in non-aqueous electrolyte: AC-voltammetry and EIS studies. *Electrochim. Acta* **2020**, *334*, 135556.
(15) Barnes, P.; Smith, K.; Parrish, R.; Jones, C.; Skinner, P.; Storch, E.; White, Q.; Deng, C.; Karsann, D.; Lau, M. L.; et al. A non-aqueous sodium hexafluorophosphate-based electrolyte degradation study: Formation and mitigation of hydrofluoric acid. *J. Power Sources* **2020**, *447*, 227363.
(16) Kennedy, L. J.; Ratnaji, T.; Konikkara, N.; Vijaya, J. J. Value added porous carbon from leather wastes as potential supercapacitor electrode using neutral electrolyte. *J. Clean Prod.* **2018**, *197*, 930−936.
(17) Chen, J.; Fang, K.; Chen, Q.; Xu, J.; Wong, C.-P. Integrated paper electrodes derived from cotton stalks for high-performance flexible supercapacitors. *Nano Energy* **2018**, *53*, 337−344.
(18) Ponce, M. F.; Mamani, A.; Jerez, F.; Castilla, J.; Ramos, P. B.; Acosta, G. G.; Sardella, M. F.; Bavio, M. A. Activated carbon from olive tree pruning residue for symmetric solid-state supercapacitor. *Energy* **2022**, *260*, 125092.
(19) Viet, D. D.; Thao, D. T.; Anh, K. D.; Tsubota, T. Autohydrolysis treatment of bamboo and potassium oxalate (K2C2O4) activation of bamboo product for CO2 capture utilization. *Front. Chem. Sci. Eng.* **2024**, *18* (4), 41.
(20) Ozpinar, P.; Dogan, C.; Demiral, H.; Morali, U.; Erol, S.; Samdan, C.; Yildiz, D.; Demiral, I. Activated carbons prepared from hazelnut shell waste by phosphoric acid activation for supercapacitor electrode applications and comprehensive electrochemical analysis. *Renewable Energy* **2022**, *189*, 535−548.
(21) Ng, S. W. L.; Yilmaz, G.; Ong, W. L.; Ho, G. W. One-step activation towards spontaneous etching of hollow and hierarchical porous carbon nanospheres for enhanced pollutant adsorption and energy storage. *Appl. Catal., B* **2018**, *220*, 533−541.
(22) Shanmuga Priya, M.; Divya, P.; Rajalakshmi, R. A review status on characterization and electrochemical behaviour of biomass derived carbon materials for energy storage supercapacitors. *Sustainable Chem. Pharm.* **2020**, *16*, 100243.
(23) Taer, E.; Yanti, N.; Apriwandi, A.; Ismardi, A.; Taslim, R. Novel O, P, S self-doped with 3D hierarchy porous carbon from aromatic agricultural waste via H3PO4 activation for supercapacitor electrodes. *Diam. Relat. Mater.* **2023**, *140*, 110415.
(24) Zhi, M.; Liu, S.; Hong, Z.; Wu, N. Electrospun activated carbon nanofibers for supercapacitor electrodes. *RSC Adv.* **2014**, *4* (82), 43619−43623.
(25) Ahmed, N.; Deng, L.; Wang, C.; Shah, Z.-u.-H.; Deng, L.; Li, Y.; Li, J.; Chachar, S.; Chachar, Z.; Hayat, F.; et al. Advancements in Biochar Modification for Enhanced Phosphorus Utilization in Agriculture. *Land* **2024**, *13* (5), 644.
(26) Hu, S.-C.; Cheng, J.; Wang, W.-P.; Sun, G.-T.; Hu, L.-L.; Zhu, M.-Q.; Huang, X.-H. Structural changes and electrochemical properties of lacquer wood activated carbon prepared by phosphoric acid-chemical activation for supercapacitor applications. *Renewable Energy* **2021**, *177*, 82−94.
(27) Zhu, Y.; Huang, Y.; Chen, C.; Wang, M.; Liu, P. Phosphorus-doped porous biomass carbon with ultra-stable performance in sodium storage and lithium storage. *Electrochim. Acta* **2019**, *321*, 134698.
(28) Benzigar, M. R.; Talapaneni, S. N.; Joseph, S.; Ramadass, K.; Singh, G.; Scaranto, J.; Ravon, U.; Al-Bahily, K.; Vinu, A. Recent advances in functionalized micro and mesoporous carbon materials: synthesis and applications. *Chem. Soc. Rev.* **2018**, *47* (8), 2680−2721.
(29) He, Y.; Zhang, Y.; Li, X.; Lv, Z.; Wang, X.; Liu, Z.; Huang, X. Capacitive mechanism of oxygen functional groups on carbon surface in supercapacitors. *Electrochim. Acta* **2018**, *282* (06.103), 618−625.
(30) Cheng, J.; Hu, S.-C.; Sun, G.-T.; Kang, K.; Zhu, M.-Q.; Geng, Z.-C. Comparison of activated carbons prepared by one-step and two-step chemical activation process based on cotton stalk for supercapacitors application. *Energy* **2021**, *215*, 119144.
(31) Villota, S. M.; Lei, H.; Villota, E.; Qian, M.; Lavarias, J.; Taylan, V.; Agulto, I.; Mateo, W.; Valentin, M.; Denson, M. Microwave-Assisted Activation of Waste Cocoa Pod Husk by H3PO4 and KOH—Comparative Insight into Textural Properties and Pore Development. *ACS Omega* **2019**, *4* (4), 7088−7095.
(32) Gueye, M.; Richardson, Y.; Kafack, F. T.; Blin, J. High efficiency activated carbons from African biomass residues for the removal of chromium(VI) from wastewater. *J. Environ. Chem. Eng.* **2014**, *2* (1), 273−281.
(33) Kong, F.; Zeng, Q.; Li, Y.; Ding, Y.; Xue, D.; Guo, X. Improving Antioxidative and Antiproliferative Properties Through the Release of Bioactive Compounds From Eucommia ulmoides Oliver Bark by Steam Explosion. *Front. Nutr.* **2022**, *9*, 916609.
(34) Bao, Q.; Zhang, M.; Li, J.; Wang, X.; Zhu, M.; Sun, G. The optimal micro- and meso-pores oriented development of Eucommia ulmoides oliver wood derived activated carbons for capacitive performance. *Renewable Energy* **2024**, *225*, 120209.
(35) Chi, Z.-Z.; Yuan, B.-X.; Qu, Q.; Zhu, M.-Q. Preparation of Eucommia ulmoides Oliver wood derived activated carbons by

https://doi.org/10.1021/acsomega.4c11529
ACS Omega 2025, 10, 15368−15380

combined microwave hydrothermal pretreatment and microwave pyrolysis as electrode materials for super capacitive performance. *Mater. Today Sustain.* **2024**, *25*, 100621.
(36) Sun, G.; Qiu, L.; Zhu, M.; Kang, K.; Guo, X. Activated carbons prepared by hydrothermal pretreatment and chemical activation of Eucommia ulmoides wood for supercapacitors application. *Ind. Crop. Prod.* **2018**, *125*, 41−49.
(37) Su, H.; Lan, C.; Wang, Z.; Zhu, L.; Zhu, M. Controllable Preparation of Eucommia Wood-Derived Mesoporous Activated Carbon as Electrode Materials for Supercapacitors. *Polymers* **2023**, *15* (3), 663.
(38) Yin, J.; Zhu, Y.; Yue, X.; Wang, L.; Zhu, H.; Wang, C. From environmental pollutant to activated carbons for high-performance supercapacitors. *Electrochim. Acta* **2016**, *201*, 96−105.
(39) Montane, D.; Tornefernandez, V.; Fierro, V. Activated carbons from lignin: kinetic modeling of the pyrolysis of Kraft lignin activated with phosphoric acid. *Chem. Eng. J.* **2005**, *106* (1), 1−12.
(40) Zhu, M. Q.; Wang, Z. W.; Wen, J. L.; Qiu, L.; Zhu, Y. H.; Su, Y. Q.; Wei, Q.; Sun, R. C. The effects of autohydrolysis pretreatment on the structural characteristics, adsorptive and catalytic properties of the activated carbon prepared from Eucommia ulmoides Oliver based on a biorefinery process. *Bioresour. Technol.* **2017**, *232*, 159−167.
(41) Fang, B.; Kim, J. H.; Kim, M.-S.; Yu, J.-S. Hierarchical Nanostructured Carbons with Meso-Macroporosity: Design, Characterization, and Applications. *Acc. Chem. Res.* **2013**, *46* (7), 1397−1406.
(42) Ma, C.; Yu, Y.; Li, Y.-j.; Shi, J.-l.; Song, Y.; Liu, L. Ion Accumulation and Diffusion Behavior in Micro-/Meso-Pores of Carbon Nanofibers. *J. Electrochem. Soc.* **2014**, *161* (9), A1330−A1337.
(43) Khalil, U.; Liu, Z.; Peng, C.; Hikichi, N.; Wakihara, T.; Garcia-Martinez, J.; Okubo, T.; Bhattacharya, S. Ultrafast surfactant-templating of *BEA zeolite: An efficient catalyst for the cracking of polyethylene pyrolysis vapours. *Chem. Eng. J.* **2021**, *412*, 128566.
(44) Meng, Q.; Gao, X.; Sun, T.; Guo, Y.; Liu, H. Aerosol-Assisted Synthesis of Sn-Si Composite Oxide Microspheres with the Hollow Mesoporous Structure for Baeyer-Villiger Oxidation. *Catalysts* **2023**, *13* (12), 1460.
(45) Wang, L.; Xie, L.; Wu, J.; Li, X.; Ma, H.; Zhou, J. Sequential H3PO4-CO2 assisted synthesis of lignin-derived porous carbon: CO2 activation kinetics investigation and textural properties regulation. *Renewable Energy* **2022**, *191*, 639−648.
(46) Valencia, A.; Muñiz-Valencia, R.; Ceballos-Magaña, S. G.; Rojas-Mayorga, C. K.; Bonilla-Petriciolet, A.; González, J.; Aguayo-Villarreal, I. A. Cyclohexane and benzene separation by fixed-bed adsorption on activated carbons prepared from coconut shell. *Environ. Technol. Innov.* **2022**, *25*, 102076.
(47) Perazzolo, V.; Durante, C.; Pilot, R.; Paduano, A.; Zheng, J.; Rizzi, G. A.; Martucci, A.; Granozzi, G.; Gennaro, A. Nitrogen and sulfur doped mesoporous carbon as metal-free electrocatalysts for the in situ production of hydrogen peroxide. *Carbon* **2015**, *95*, 949−963.
(48) Wang, J.; Kaskel, S. KOH activation of carbon-based materials for energy storage. *J. Mater. Chem.* **2012**, *22* (45), 23710.
(49) Zhao, Z.; Chen, H.; Zhang, W.; Yi, S.; Chen, H.; Su, Z.; Niu, B.; Zhang, Y.; Long, D. Defect engineering in carbon materials for electrochemical energy storage and catalytic conversion. *Mater. Adv.* **2023**, *4* (3), 835−867.
(50) Ma, M.; Cai, W.; Chen, Y.; Li, Y.; Tan, F.; Zhou, J. Flower-like NiMn-layered double hydroxide microspheres coated on biomass-derived 3D honeycomb porous carbon for high-energy hybrid supercapacitors. *Ind. Crop. Prod.* **2021**, *166*, 113472.
(51) Shahrivar, J.; Gharabaghi, M. Separation of AuCN2- by activated carbon and functionalized graphene/activated carbon composite. *Adv. Powder Technol.* **2020**, *31* (12), 4648−4656.
(52) Zhang, S.; Wang, L.; Zhang, Y.; Cao, F.; Sun, Q.; Ren, X.; Wennersten, R. Effect of hydroxyl functional groups on SO2 adsorption by activated carbon. *J. Environ. Chem. Eng.* **2022**, *10* (6), 108727.
(53) Tan, X. F.; Liu, S. B.; Liu, Y. G.; Gu, Y. L.; Zeng, G. M.; Hu, X. J.; Wang, X.; Liu, S. H.; Jiang, L. H. Biochar as potential sustainable precursors for activated carbon production: Multiple applications in environmental protection and energy storage. *Bioresour. Technol.* **2017**, *227*, 359−372.
(54) Alhebshi, N. A.; Salah, N.; Hussain, H.; Salah, Y. N.; Yin, J. Structural and Electrochemical Properties of Physically and Chemically Activated Carbon Nanoparticles for Supercapacitors. *Nanomaterials* **2022**, *12* (1), 122.
(55) Jaouadi, M.; Marzouki, M.; Hamzaoui, A. H.; Ghodbane, O. Enhanced electrochemical performance of olive stones-derived activated carbon by silica coating for supercapacitor applications. *J. Appl. Electrochem.* **2022**, *52* (1), 125−137.
(56) Wang, C.; Bai, L.; Zhao, F.; Bai, L. Activated carbon fibers derived from natural cattail fibers for supercapacitors. *Carbon Lett.* **2022**, *32* (3), 907−915.
(57) Gupta, G. K.; Sagar, P.; Pandey, S. K.; Srivastava, M.; Singh, A. K.; Singh, J.; Srivastava, A.; Srivastava, S. K.; Srivastava, A. In Situ Fabrication of Activated Carbon from a Bio-Waste Desmostachya bipinnata for the Improved Supercapacitor Performance. *Nanoscale Res. Lett.* **2021**, *16* (1), 85.
(58) Karnan, M.; Subramani, K.; Srividhya, P. K.; Sathish, M. Electrochemical Studies on Corncob Derived Activated Porous Carbon for Supercapacitors Application in Aqueous and Non-aqueous Electrolytes. *Electrochim. Acta* **2017**, *228*, 586−596.
(59) Eleri, O. E.; Huld, F.; Pires, J.; Tucho, W. M.; Schweigart, P.; Svensson, A. M.; Lou, F.; Yu, Z. Revealing mechanisms of activated carbon capacity fade in lithium-ion capacitors. *Electrochim. Acta* **2023**, *453*, 142359.
(60) Shin, S.; Shin, M. W. Nickel metal−organic framework (Ni-MOF) derived NiO/C@CNF composite for the application of high performance self-standing supercapacitor electrode. *Appl. Surf. Sci.* **2021**, *540*, 148295.
(61) Genel, I.·.; Yardım, Y.; Saka, C. Utilisation of green nitrogen-doped biomass-based hierarchical porous activated carbon particles for enhancement of electrochemical energy storage performance. *Diam. Relat. Mater.* **2025**, *152*, 111912.
(62) Fan, Q.; Song, C.; Zhang, Y.; Ren, G.; Sun, Y.; Fu, P. Biomass-based porous carbon with surface grown MXenes for high-performance electromagnetic absorption and supercapacitor validated from structural and charge changes. *J. Mater. Sci.* **2023**, *58* (44), 17045−17065.
(63) Li, S.; Yang, J.; Wang, H.; Chen, L. A High Yield and Cost-Effective Pathway for the Production of Iron Doped Porous Carbon Derived from Squid Pen as Supercapacitor Electrode Material. *Waste Biomass Valorization* **2023**, *14* (9), 2815−2824.
(64) Li, T.; Wei, X.; Zhang, Y.; Cai, Y.; Chen, X.; Xu, Y. Ti3C2Tx/CDs@MnO2 composite as electrode materials for supercapacitors: synthesis and electrochemical performance. *Ionics* **2024**, *30* (10), 6413−6423.
(65) Raj, R.; Iqbal, M.; Singh, G. P.; Haldar, K. K. Enhancing Electrochemical Performance through Li2Mn3ZnO8 Integration into Ti3C2Tx MXene Nanocomposites for Advanced Supercapacitors and Hydrogen Evolution Reactions. *Adv. Eng. Mater.* **2024**, *26* (22), 2401647.
(66) Veann, C.; Sichumsaeng, T.; Kalawa, O.; Chanlek, N.; Kidkhunthod, P.; Maensiri, S. Structure and electrochemical performance of delafossite AgFeO2 nanoparticles for supercapacitor electrodes. *Int. J. Miner. Metall. Mater.* **2025**, *32* (1), 201−213.
(67) Kumar Jha, M.; Shah, D.; Mulmi, P.; Joshi, S.; Kumar Sharma, R.; Pant, B.; Park, M.; Raj Pant, H. Development of activated carbon from bhang (Cannabis) stems for supercapacitor electrodes. *Mater. Lett.* **2023**, *344*, 134436.
(68) Cui, G.; Wang, R.; Guan, Y.; Li, J.; Li, Y.; Zhao, Y.; Wang, H. In-situ electropolymerized polyaniline nanoparticles grown on longan shell-derived porous carbon for high-performance supercapacitor electrode. *J. Electroanal. Chem.* **2024**, *963*, 118293.
(69) Liu, C.; Wang, L.; Xia, Z.; Chen, R.; Wang, H.-L.; Liu, Y. Carbon hollow fibers with tunable hierarchical structure as self-standing supercapacitor electrode. *Chem. Eng. J.* **2022**, *431*, 134099.

https://doi.org/10.1021/acsomega.4c11529
ACS Omega 2025, 10, 15368−15380

(70) Long, Y.; An, X.; Zhang, H.; Yang, J.; Liu, L.; Tian, Z.; Yang, G.; Cheng, Z.; Cao, H.; Liu, H.; et al. Highly graphitized lignin-derived porous carbon with hierarchical N/O co-doping "core-shell" superstructure supported by metal-organic frameworks for advanced supercapacitor performance. *Chem. Eng. J.* **2023**, *451*, 138877.
(71) Jiao, S.; Zhang, L.; Li, C.; Zhang, H.; Zhang, J.; Li, P.; Tao, Y.; Zhao, X.; Chen, H.; Jiang, J. Efficient construction of a carbon-based symmetric supercapacitor from soybean straw by coupling multi-stage carbonization and mild activation. *Ind. Crop. Prod.* **2022**, *183*, 114906.
(72) Ahmad, T.; Murtaza; Shah, S. S.; Khan, S.; Khan, A. A.; Ullah, N.; Oyama, M.; Aziz, M. A. Preparation and electrochemical performance of Convolvulus arvensis-derived activated carbon for symmetric supercapacitors. *Mater. Sci. Eng., B* **2023**, *292*, 116430.

https://doi.org/10.1021/acsomega.4c11529
ACS Omega 2025, 10, 15368−15380